A 3D finite element stochastic framework for the failure of tow-based discontinuous composites

M. Alves[a,1], L. M. Martulli[b,c,1], M. Kerschbaum[b], Y. Swolfs[c], S. Lomov[c], S. Pimenta[a,*]

[a] *meComposites, Mechanical Engineering Department, Imperial College London, South Kensington Campus, London, SW7 2AZ, UK*
[b] *Toyota Motor Europe, B-1930 Zaventem, Belgium*
[c] *Department of Materials Engineering, KU Leuven, Kasteelpark Arenberg 44 bus 2450, Belgium*

Abstract

Tow-Based Discontinuous Composites (TBDCs) combine high manufacturability with good mechanical properties. This work presents a novel 3D approach for the numerical modelling of TBDCs. The framework generates 3D orientation tensors by adding a stochastic component to the orientation tensors deterministically predicted by a process simulation. The actual TBDCs are thus idealised as Equivalent Laminates (ELs), resulting from these stochastic tensors. A physically based 3D failure criterion is presented for the prediction of failure initiation of the ELs. The consequent stiffness reduction is captured by a ply-discount method. The approach is validated for two TBDCs materials, with two different moulding conditions and different amounts of in-mould flow. The proposed approach accurately predicts the characteristic variability of these materials. As a consequence, the predicted strength was in good agreement with the experimental results of both materials tested.

Keywords: A. Short-fibre composites; C.Finite Element Analysis (FEA); C.Material modelling; C.Multiscale modelling; B. Strength

1. Introduction

Tow Based Discontinuous Composites (TBDCs) are a class of discontinuous composites composed of chopped carbon-fibre tows distributed in a polymeric matrix. This microstructure allows for high fibre content and high aspect ratio, which both lead to high values of stiffness and toughness [1–4]; moreover, the discontinuous nature of the microstructure of TBDCs confers good formability, enabling them to be moulded by automated processes and at high-volume production rates. The combination of good performance and manufacturability makes TBDCs very appealing for several high-volume applications, as they are also significantly cheaper than conventional continuous fibre composites.

A widespread use of TBDCs in structural application is currently hindered by the lack of reliable analytical or numerical models. The stochastic nature of the complex TBDCs microstructure, which

*Corresponding author
Email address: soraia.pimenta@imperial.ac.uk (S. Pimenta)
[1] These authors share the first co-authorship. LMM is now employed at Politecnico di Milano.

depends on the influence of in-mould flow during manufacturing, makes the creation of accurate and computationally efficient models a difficult task. Numerical models were developed that explicitly represent both tows and matrix in a Representative Volume Element (RVE) [5–9]. In particular, Harper et al. [6] have used a microstructure generator to construct RVEs with different volume fractions and tow geometries. When used in Finite Element (FE) simulations, those RVEs predicted the tensile stiffness and strength with less than 5% discrepancy compared to experimental values; compressive and shear moduli and strength were also predicted, but with larger discrepancies. A similar approach was adopted by Chen et al [5]: they created different RVEs with a microstructure generator, with different global orientation, ranging from fully aligned to complete random isotropic. Both tensile stiffness and strength were in good agreement with experimental data. Li et al. [7] constructed their RVEs by inspecting TBDCs micrographs, therefore requiring material tests as input to the model. Stelzer et al. [9] also constructed several RVEs using the commercial software Digimat [10] and information extracted from a tensile specimen scanned via micro-Computed Tomography (μCT). The software could use input data to generate stochastic RVEs, thus allowing for the stochastic nature of the material to be reproduced.

These works [5–9] achieve a good prediction accuracy of mechanical performance. However, these models rely on explicit reconstructions of the material's microstructure; this limits their applicability to simple geometries, while requiring high computational resources. This hinders their use for industrial design, which requires models that offer the flexibility to be used efficiently for both simple and more complex geometries.

Feraboli et al. [11] discretised a 2D specimen in a series of random analytical RVEs; the size of the RVEs was defined from experimental strain fields, and each RVE was modelled as a 2D stochastic equivalent laminate. The idea was combined with a 2D structure generator by Selezneva et al. [12]; although the FE simulations did not model the tows and the matrix explicitly, the use of a 2D microstructure generator and of a 2D model makes such an approach impractical for real-life applications.

Alves et al. [13] proposed the concept of characteristic length-scale of a TBDC as the intrinsic material property governing its spatial variability. They measured the characteristic length-scale experimentally by creating a triangulation of peaks and troughs on elastic strain fields (obtained through DIC of unnotched tensile specimens) of a TBDC, and equating the characteristic length-scale to the average segment length in that triangulation. This effectively defines the characteristic length-scale as the average distance between uncorrelated elastic properties in a TBDC material. FE models based on an explicit representation of the tows have revealed that the characteristic length-scale of a TBDC could be approximated as the harmonic mean of the tow length and width.

Alves et al. [8] proposed a fully-implicit 2D stochastic FE framework for TBDCs, which successfully reproduces the spatial variability of strain fields that is characteristic of these materials, and which has been applied to simulate actual components [14, 15]. The framework is based on the concept of "characteristic lengths-scale" introduced in the previous paragraph, and of Stochastic Equivalent Laminates (SELs, i.e. lay-ups of unidirectional discontinuous plies with random in-plane orientations). For each FE simulation, the framework generates uncorrelated SELs at discrete seed points, which are separated from one-another by the characteristic length-scale; the stochastic orientation tensors of these stochastic ELs are then interpolated to the integration points of the finite elements, which creates smooth and heterogeneous 2D strain fields similar to experimental ones (i. e. with the same characteristic lengths-scale and similar variability of strength values). However, this framework was not coupled with compression-moulding process simulations, and therefore was not tested for materials with preferential fibre alignment; it was also limited to a 2D implementation (i.e. planar or shell-based, suitable for thin structures only), and did not consider failure and damage propagation.

Li and Pimenta [16] proposed an analytical model for Equivalent Laminates (ELs) of TBDCs. This model was strictly valid for the average stiffness of a specimen, but the EL strength was higher than the TBDC due to a much larger variability in the latter [17]; this highlights the importance of considering variability when simulating TBDC structures. This model [16] was based on a 2D formulation, and it was thus limited to thin structures. A random in-plane isotropic orientation was also assumed, and the effects of the compression moulding on the tow orientations were not considered, which is not suitable for complex parts. Moreover, the model could not reproduce any damage accumulation and propagation mechanisms leading to failure.

Kravchenko et al. [18] explicitly modelled the tows in a voxel-based FE approach. Different meso-structures were created by a random generator. Intra-tow and inter-tow damage were considered. This approach was extended to model tow debonding using cohesive elements by Sommer et al. [19]. Moreover, the authors coupled compression moulding simulations with the structural analysis to consider the process-induced effects morphological effects on a TBDC. The process simulations were based on an earlier work [20]. While strength and stiffness predictions were quite accurate, both process and structural simulations are based on an explicit model of the entire meso-structure (matrix and tows). This limits significantly the versatility and scalability of the model to larger, more complex components.

Görthofer et al. [21] also proposed to couple process and structural simulations. The authors also included μCT scans in the simulation chain to accurately measure the local tow orientation. The failure modes considered in the structural model were mainly matrix cracking and tow debonding. The model was validated against a demonstrator, showing good predictive capabilities.

Overall, very few models can be effectively used in industrial design of TBDC parts, while considering the effects of the manufacturing on their performance. Therefore, in this work, a new stochastic FE framework for TBDC simulations is proposed. The framework is based on a simulation chain involving process simulations, a stochastic assignment of 3D material properties and the structural simulation itself. The compression moulding simulation is used to predict the orientation of the tows induced by the in-mould flow of uncured material. Section 2 describes the two TBDC material systems tested under longitudinal tension. Section 3 presents the different modules of the framework: (i) the coupling with fibre orientation results from process simulations; (ii) the assignment of 3D stochastic material properties; and (iii) the development of a 3D physically-based failure criterion and stiffness reduction scheme used to predict final failure. The results of the framework are compared against the experimental results in Section 4, and are discussed in Section 5. The main conclusions of this work are summarised in Section 6.

2. Materials and methods

In this work, two TBDCs material systems will be used for the experimental validation of the proposed framework:

1) HexMC-M77 [22], a commercially available TBDC material system from Hexcel Corporation: the TBDC plates were manufactured with a charge coverage $\geq 80\%$, and therefore correspond to a low-flow material system. This results in quasi-in-plane isotropic properties due to the uniformly random tow orientation. Manufacturing and testing of the randomly-oriented TBDC specimens is described in [13].

2) STR120N [23], a Carbon Fibre Sheet Moulding Compound (CF-SMC) provided by Mitsubishi Chemical Carbon Fiber and Composites GmbH: the CF-SMC plates were manufactured with a charge coverage of 20%, and therefore correspond to a high-flow material. Manufacturing and testing of the oriented CF-SMC specimens is described in [24]. Specimens were then waterjet cut from the plates at an angle with the main flow direction of 0°, 45° and 90°. In the rest of this paper, they will be referred to as "0°", "45°" and "90°" CF-SMC specimens, respectively.

Details of the charge shape and location for both cases are provided in Appendix A. The microstructural features of each material system described above are defined in Table 1. Overall, the major difference between the two materials is the amount of flow present during moulding.

The HexMC-M77 and the CF-SMC specimens were both tested under longitudinal tension according to the ASTM D3039 standard [25]; the specimens geometry of each material system is defined in

TABLE 1: Specification of the microstructural elements (tow length l^{t}, tow width w^{t}, tow thickness t^{t} and fibre volume fraction V^{f}) of the material systems analysed; dimensions are in mm and volume fractions in %.

Material	l^{t}	w^{t}	t^{t}	V^{f}
HexMC-M77 [8, 22]	50.0	8.0	0.125	57
CF-SMC [23]	25.0	8.0	0.15	42

Table 3. A displacement rate of 1 mm/min was used. Digital Image Correlation (DIC) was used to measure the strain fields on the surface of each specimen.

3. FE framework development

The proposed framework has the modular implementation represented in Figure 1. The different modules are described below:

1) Process simulation: a compression moulding simulation is performed to evaluate the process-induced fibre orientations. The fibre orientations are described by second order orientation tensors $\mathbf{a}$ [26]. More details on this step are presented in Appendix A.

2) Spatial variability and local assignment of stochastic properties: the second order fibre orientation tensors $\mathbf{a}$ resulting from the process simulation are mapped to seed points in a seeds mesh (as shown in Figure 2), with a nominal distance between seeds equal to the characteristic spacing given by the harmonic mean between the tow length and width [13]. A stochastic process is used to convert each nominal local orientation tensor $\mathbf{a}$ at the seed points to a stochastic orientation tensor $\bar{\mathbf{a}}$. These stochastic tensors are then interpolated from the seed points to the centroids of the finite elements of a refined *structural mesh* used in the structural FE simulation. Details of this module are described in Section 3.1. The use of an intermediate seed mesh thus allows to model the stochastic nature of TBDCs. A different approach, more commonly used for short fibre composites, is to map the fibre orientation obtained in the process simulation directly on the structural mesh. This approach, referred to in this work as *Deterministic FE* and also shown in Figure 2, will also be tested to demonstrate the improvement given by the proposed stochastic approach.

3) Material model and structural FE simulation: the TBDC material is idealised as Equivalent Laminates (ELs), generated from the stochastic orientation tensors. The failure initiation of the ELs is evaluated using a new 3D failure criterion, and the consequent stiffness reduction is modelled by a ply discount method. Details of this module are described in Section 3.2.

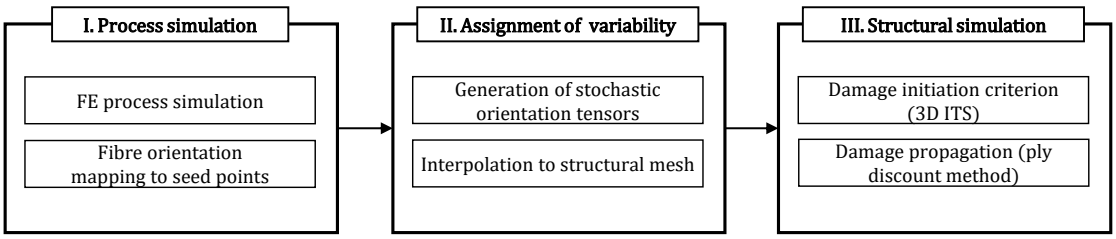

Figure 1: The modular implementation of the stochastic framework.

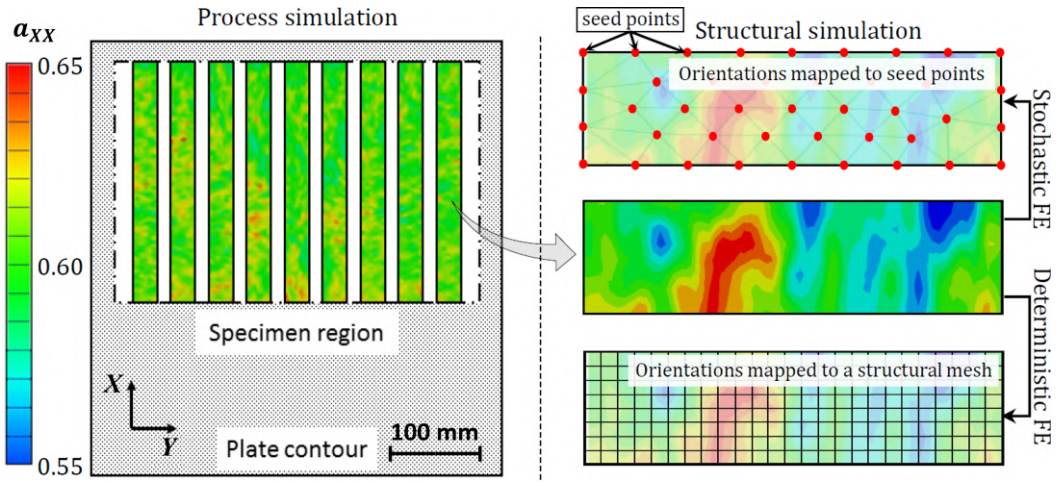

Figure 2: The mapping of orientation tensors **a** resulting from the process simulation to the seed points used in the stochastic FE framework. The direct mapping of the **a** to each element of the structural mesh is also shown, and used in a deterministic FE approach (described in Section 4). The orientation tensor component a_{XX} is shown on the surface for the process simulation (on the left), while it is averaged through the thickness for the specimens meshes (on the right).

3.1. 3D assignment of stochastic mechanical properties

3.1.1. Coordinate systems definition

Tows are assumed to remain mostly planar (possibly with a minor out-of-plane component) entities after the compression moulding process. Martulli et al. [24] reported, for the high-flow CF-SMC material considered, the presence of swirls and other losses of tow planarity, as also observed in the literature [27, 28]. However, these were found to be mainly localised feature, often not leading to final failure, while the overall planarity of the tows was preserved [24]. On the other hand, swirls were never observed when limited material flow is involved during manufacturing [29], as for the HexMC-M77 material. As a result of this assumption, the local ELs are characterised by an average out-of-plane orientation (characterised by the angle ϕ^{EL} to be defined in Eq. 4), and an in-plane orientation distribution (as will be explained in the paragraph just before Eq. 4). Three different coordinate systems are used in the process of assigning stochastic mechanical properties (shown in figure 3):

1) Global coordinate system $\mathrm{CSYS}^{\mathrm{g}}$, with axis (XYZ) - this is the global coordinate system of the FE simulation.

2) Equivalent laminate coordinate system CSYS^{EL}, with axis (xyz) - this is the coordinate system in which the ELs resulting from the stochastic orientation tensors are generated. It is obtained by aligning the Z axis of CSYS^{g} with the direction normal to the local plane of the tows z, as described in Section 3.1.2. The angle between Z and z is γ, as shown in Figure 3.

3) Local coordinate system CSYS^{l}, with axis (123) - this is the local coordinate system of each discontinuous ply of the EL, in which direction 1 is aligned with the fibre direction, direction 2 defines the transverse direction and direction 3 coincides with z.

The coordinate system in which a variable is expressed will hereafter be represented by superscripts 'g', 'EL', or '123'.

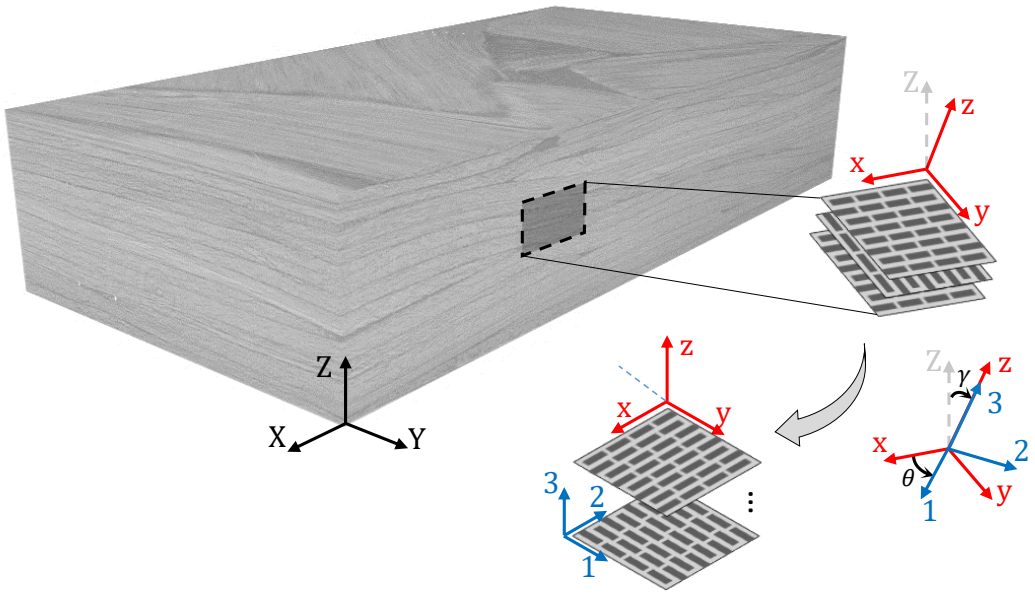

Figure 3: The three different coordinate systems CSYS defined in the FE framework.

3.1.2. 3D stochastic orientation tensors

The second order orientation tensors $\mathbf{a}^{g}$ resulting from the process simulations and mapped to the seed points are defined in the global coordinate system CSYS^{g}. To generate an EL, a planar Fibre Orientation Distribution (FOD) function in CSYS^{EL} is required (as will be explained in Section 3.2.1), and, therefore, the orientation tensors $\mathbf{a}^{g}$ have to be expressed in CSYS^{EL} ($\mathbf{a}^{EL}$).

The unit-length eigenvectors ($\mathbf{e}_1$, $\mathbf{e}_2$ and $\mathbf{e}_3$) of $\mathbf{a}^{g}$, define the principal directions of fibre orientation; the eigenvalues (λ_1, λ_2 and λ_3) indicate the statistical proportions of fibres oriented along those directions. The directional vector of axis z of CSYS^{EL} is defined by the eigenvector $\mathbf{e}_3$, which is associated with the smallest eigenvalue λ_3. The angle γ between the directional vectors $\mathbf{e}_3$ and $\mathbf{Z}$

(which is defined by (0,0,1) in the CSYS$^{\mathrm{g}}$), as shown in Figure 3, is given by

$$\gamma = \arccos(e_3^{\mathrm{z}}), \tag{1}$$

where e_3^Z is component of the third eigenvector along the $\mathbf{Z}$ axis. The coordinate transformation matrix $\mathbf{T}_{\mathrm{g/EL}}$ from CSYS$^{\mathrm{g}}$ to CSYS$^{\mathrm{EL}}$ is defined by a rotation around an axis $\mathbf{u}$ and by the angle γ. The axis of rotation $\mathbf{u}$ (perpendicular to both e_3^Z and $\mathbf{Z}$) is given by $\mathbf{u} = \mathbf{e}_3 \times \mathbf{Z}$; and the transformation matrix $\mathbf{T}_{\mathrm{g/EL}}$ is finally defined as [30]:

$$\mathbf{T}_{\mathrm{g/EL}} = \begin{bmatrix} \cos\gamma + {u^X}^2 (1-\cos\gamma) & u^X u^Y (1-\cos\gamma) - u^Z \sin\gamma & u^X u^Z (1-\cos\gamma) + u^Y \sin\gamma \\ u^Y u^X (1-\cos\gamma) + u^Z \sin\gamma & \cos\gamma + {u^Y}^2 (1-\cos\gamma) & u^Y u^Z (1-\cos\gamma) - u^X \sin\gamma \\ u^Z u^X (1-\cos\gamma) - u^Y \sin\gamma & u^Z u^Y (1-\cos\gamma) + u^X \sin\gamma & \cos\gamma + {u^Z}^2 (1-\cos\gamma) \end{bmatrix}. \tag{2}$$

This definition of $\mathbf{T}_{\mathrm{g/EL}}$ was chosen out of convenience, since it allows an easier extraction of the planar FOD and its principal directions.

The orientation tensor $\mathbf{a}^{\mathrm{g}}$ can therefore be represented in the CSYS$^{\mathrm{EL}}$ by the following transformation:

$$\mathbf{a}^{\mathrm{EL}} = \mathbf{T}_{\mathrm{g/EL}} \mathbf{a}^{\mathrm{g}} \mathbf{T}_{\mathrm{g/EL}}^{-1}. \tag{3}$$

The use of the cross-product $\mathbf{e}_3 \times \mathbf{Z}$ in the definition of $\mathbf{u}$, can lead to inaccuracies when $\mathbf{e}_3$ and $\mathbf{Z}$ are aligned. To avoid this problem, for values of $\gamma \leq 0.1^\circ$ it is assumed that the coordinate systems CSYS$^{\mathrm{EL}}$ and CSYS$^{\mathrm{g}}$ are coincident.

The recovery of the FOD from the $\mathbf{a}^{\mathrm{EL}}$ requires the knowledge of the associated fourth-order orientation tensor $\mathbf{A}^{\mathrm{EL}}$; the latter is obtained from the $\mathbf{a}^{\mathrm{EL}}$ using an orthotropic closure approximation [31]. In Figure 4a, an example of a FOD $\mathcal{F}(\theta, \phi)$ (where ϕ is the angle between a fibre and the z- or $\mathbf{Z}$-axis, and θ is the angle between a fibre and the x- or $\mathbf{X}$-axis in the xy or XY-plane) reconstructed from a generic $\mathbf{a}^{\mathrm{g}}$ is shown, and the same $\mathcal{F}(\theta, \phi)$ defined in CSYS$^{\mathrm{EL}}$ is represented in Figure 4b. This procedure is described in [26], where a similar example on a planar FOD is present.

To generate a stochastic orientation tensor in this reference system $\bar{\mathbf{a}}^{\mathrm{EL}}$, N^{t} in-plane orientations θ_i^{EL} are randomly sampled from the normalised planar orientation distribution function $\mathcal{F}^{\mathrm{EL}}(\theta, \frac{\pi}{2})$, which is highlighted in Figure 4b. The value of N^{t} here is taken as a physical parameter which represents the tow count in the thickness direction – given by the ratio of the local thickness of the geometry to be modelled and the nominal tow thickness (in case of a flat specimen $N^{\mathrm{t}} = t^{\mathrm{s}}/t^{\mathrm{t}}$). The

characteristic out-of-plane orientation ϕ^{EL} can be calculated from $\mathbf{a}^{\mathrm{EL}}$ by,

$$\phi^{\mathrm{EL}} = \arccos(\sqrt{a_{33}^{\mathrm{EL}}}). \tag{4}$$

The stochastic orientation tensor $\bar{\mathbf{a}}^{\mathrm{EL}}$ can therefore be reconstructed based on the N^{t} sampled in-plane orientations θ_i and from the characteristic out-of-plane orientation ϕ^{EL} from

$$\bar{\mathbf{a}}^{\mathrm{EL}} = \frac{1}{N^{\mathrm{t}}} \cdot \sum_{i=1}^{N^{\mathrm{t}}} \begin{bmatrix} \sin^2(\phi^{\mathrm{EL}})\cos^2(\theta_i) & \sin^2(\phi^{\mathrm{EL}})\cos(\theta_i)\sin(\theta_i) & \sin(\phi^{\mathrm{EL}})\cos(\phi^{\mathrm{EL}})cos(\theta_i) \\ \sin^2(\phi^{\mathrm{EL}})\cos(\theta_i)\sin(\theta_i) & \sin^2(\phi^{\mathrm{EL}})\sin^2(\theta_i) & \sin(\phi^{\mathrm{EL}})\cos(\phi^{\mathrm{EL}})\sin(\theta_i) \\ \sin(\phi^{\mathrm{EL}})\cos(\phi^{\mathrm{EL}})cos(\theta_i) & \sin(\phi^{\mathrm{EL}})\cos(\phi^{\mathrm{EL}})\sin(\theta_i) & \cos^2(\phi^{\mathrm{EL}}) \end{bmatrix}. \tag{5}$$

To transform the $\bar{\mathbf{a}}^{\mathrm{EL}}$ back to the global coordinate system, the following transformation is done

$$\bar{\mathbf{a}}^{\mathrm{g}} = \mathbf{T}_{\mathrm{g/EL}}^{-1} \bar{\mathbf{a}}^{\mathrm{EL}} \mathbf{T}_{\mathrm{g/EL}}. \tag{6}$$

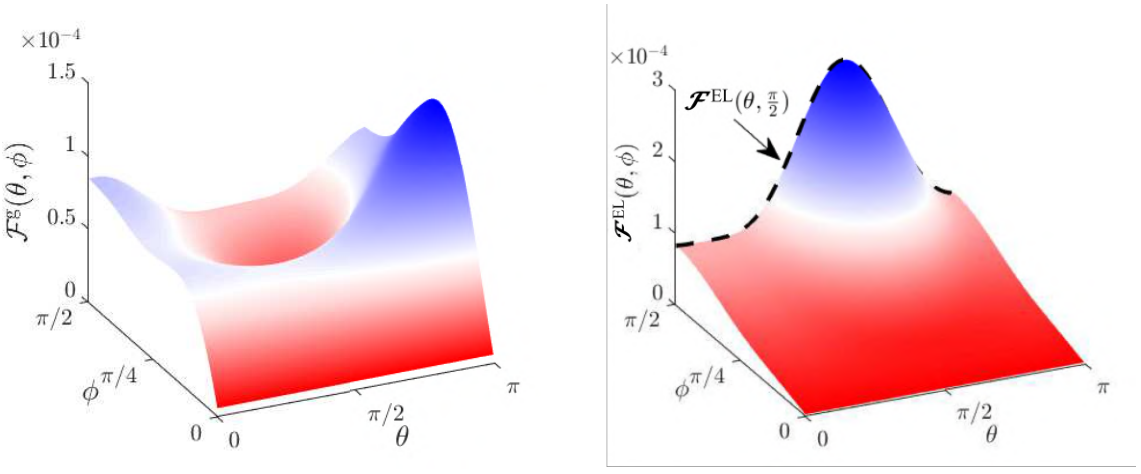

(a) Reconstruction of the 3D FOD in CSYS$^{\mathrm{g}}$.

(b) Reconstruction of the 3D FOD in CSYS$^{\mathrm{EL}}$.

Figure 4: Transformation of the FOD function in from the global to the EL reference system; representation of $\mathcal{F}^{\mathrm{EL}}(\theta, \frac{\pi}{2})$, highlighted by the dashed-line in Figure 4b.

Overall, the generation of stochastic orientation tensors requires the orientation tensors $\mathbf{a}^{\mathrm{g}}$ resulting from the process simulation and the tow count N_t in the thickness direction.

3.1.3. Interpolation of the stochastic orientation tensor from the seeds to the structural mesh

The structural simulation will be carried out in a more refined structural mesh (i.e. with an average element size significantly smaller than the average spacing between the EL seeds); this requires the definition of the stiffness tensor at the integration points of the element of the structural mesh. Using the interpolation scheme presented in [13], each term of the stochastic orientation tensor $\bar{\mathbf{a}}^{\mathrm{g}}$ is interpolated from the seed points to the centroid of the refined mesh's elements.

The stiffness tensor for each element of the structural mesh $\mathbf{C}^{\mathrm{g}}_{\mathrm{TBDC}}$ is calculated using the orientation averaging scheme presented by Advani and Tucker [26]. This requires the definition of the stiffness tensor of a UD discontinuous ply $\mathbf{C}_{\mathrm{D}}$ (see Appendix B), as well and the interpolated second order stochastic orientation tensor and the respective fourth order tensor.

The implementation of the stochastic FE framework is done in Abaqus via a Python script; the steps of the implementation are summarised in the flow-chart of Figure 5.

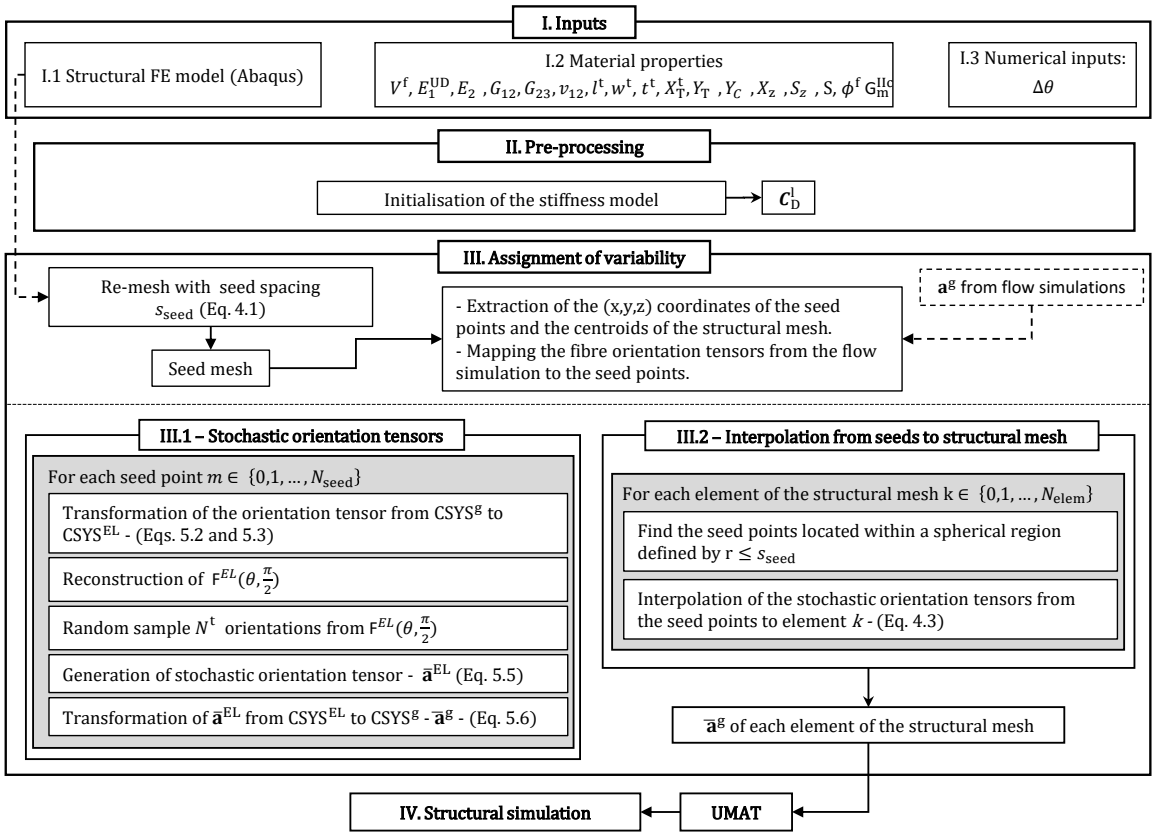

Figure 5: Implementation flowchart of the stochastic framework.

3.2. Failure criterion for an equivalent UD discontinuous ply

3.2.1. Stress transformation to the equivalent laminae

Following the EL analogy, failure prediction requires the knowledge of the stress state at each ply. Since the terms of $\bar{\mathbf{a}}^{\mathrm{g}}$ are interpolated from the seed points to each element of the structural mesh, a stacking sequence associated to each element can be reconstructed based on the respective planar FOD $\mathcal{F}^{\mathrm{EL}}(\theta,\frac{\pi}{2})$. For this purpose, $\mathcal{F}^{\mathrm{EL}}(\theta,\frac{\pi}{2})$ (whose reconstruction from $\bar{\mathbf{a}}$ is detailed in Section 3.1.2) is discretised in $N_\theta = \pi/\Delta\theta$ increments, each $\Delta\theta$ wide, as shown in Figure 6. Consider an interval centred at θ^* and bounded by the angles $\theta^* - \Delta\theta/2$ and $\theta^* + \Delta\theta/2$. The area r_{θ^*} below the $\mathcal{F}^{\mathrm{EL}}(\theta,\frac{\pi}{2})$, bounded by those angles, represents the probability of a UD discontinuous ply having an in-plane orientation within the interval $\Delta\theta$ centred in θ^*. Since the total area below $\mathcal{F}^{\mathrm{EL}}(\theta,\frac{\pi}{2})$ is 1,

the probability r_{θ^*} can be used to assign the relative frequency of having plies in the EL with an in-plane orientation θ^*:

$$N_{ply}(\theta^*) = r_{\theta^*} = \mathcal{F}^{\mathrm{EL}}(\theta^*, \frac{\pi}{2}) \cdot \Delta\theta. \tag{7}$$

The full stacking sequence is obtained by repeating this procedure for all the angle intervals N_θ in which $\mathcal{F}^{\mathrm{EL}}(\theta, \frac{\pi}{2})$ is discretised.

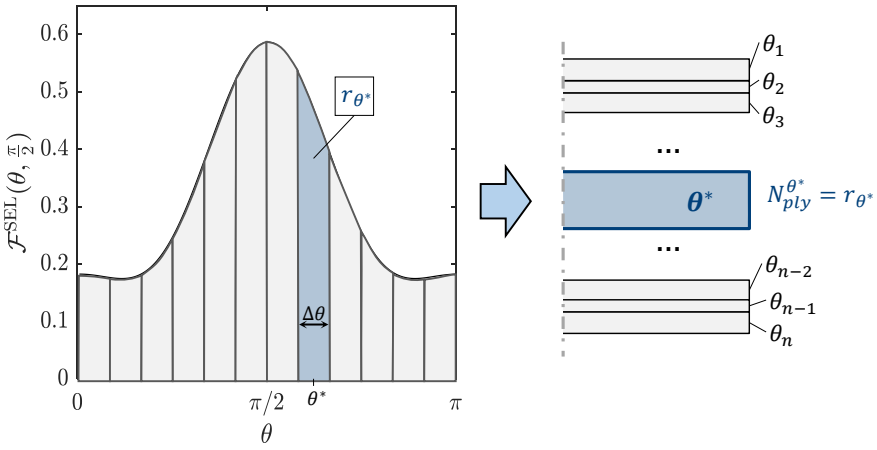

Figure 6: Discretisation of the $\mathcal{F}^{\mathrm{EL}}(\theta, \frac{\pi}{2})$ and stacking sequence reconstruction.

Once the stacking sequence is obtained, the global strain applied $\boldsymbol{\epsilon}^{\mathrm{g}}$ is expressed in the local coordinate system of each angle interval centered at θ_i:

$$\boldsymbol{\epsilon}^{\mathrm{l}}(\phi_i) = \mathbf{T}_{\theta_i}^{-1} \left(\mathbf{T}_{\mathrm{g/EL}}^{-1} \, \boldsymbol{\epsilon}^{\mathrm{g}} \, \mathbf{T}_{\mathrm{g/EL}} \right) \mathbf{T}_{\theta_i} = \mathbf{T}_{\theta_i}^{-1} \, \boldsymbol{\epsilon}^{\mathrm{EL}} \, \mathbf{T}_{\theta_i} \tag{8}$$

where $\mathbf{T}_{\theta_i}$ is the transformation matrix from CSYS$^{\mathrm{EL}}$ to CSYS$^{\mathrm{l}}$ of each ply oriented at θ_i, given by,

$$\mathbf{T}_{\theta_i} = \begin{bmatrix} \cos\theta_i & -\sin\theta_i & 0 \\ \sin\theta_i & \cos\theta_i & 0 \\ 0 & 0 & 1 \end{bmatrix} \tag{9}$$

Using the stiffness tensor for a UD discontinuous ply ($\mathbf{C}_{\mathrm{D}}$, see Appendix B) obtained in Section 3.1.3, the local stress field $\boldsymbol{\sigma}^l$ in the $N_{\mathrm{ply}}(\theta_i)$ plies with orientation θ_i is then given by:

$$\boldsymbol{\sigma}^l(\theta_i) = \mathbf{C}_{\mathrm{D}}^{\mathrm{l}} \boldsymbol{\epsilon}^{\mathrm{l}}(\theta_i). \tag{10}$$

Note that this formulation does not account for the position of each ply in the through-the-thickness direction.

3.2.2. 3D Failure criterion for a discontinuous equivalent lamina

The interactive tensile-shear (ITS) failure criterion presented in [16] is here used to assess failure due to the interaction between the in-plane stresses: i.e longitudinal-tension (σ_1), transverse-tension (σ_2) and in-plane shear (τ_{12}). To increase to computational efficiency of the implementation of the model, the ITS failure surface [16] is approximated by the following analytical expression:

$$\frac{{\sigma_1}^2}{{X_{\mathrm{T}}^{\mathrm{D}}}^2} + \frac{{\sigma_2}^2}{{Y_{\mathrm{is,T}}}^2} + \frac{{\tau_{12}}^2}{{S_{\mathrm{is}}}^2} = 1 \tag{11}$$

where $X_{\mathrm{T}}^{\mathrm{D}}$ is the tensile strength of a UD discontinuous ply, $Y_{\mathrm{is,T}}$ and S_{is} are the respective in-situ tensile and shear strengths [32]. This failure surface defines an in-plane failure index F_{ip}. For a generic

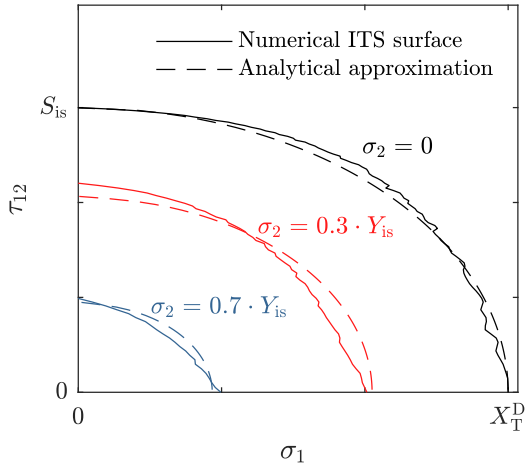

Figure 7: Comparison between the numerical and the approximated ITS failure surface.

stress field $\boldsymbol{\sigma}$, an in-plane failure index F_{ip} can be defined by

$$F_{\mathrm{ip}} = \sqrt{\frac{{\sigma_1}^2}{{X_{\mathrm{T}}^{\mathrm{D}}}^2} + \frac{{\sigma_2}^2}{{Y_{\mathrm{is,T}}}^2} + \frac{{\tau_{12}}^2}{{S_{\mathrm{is}}}^2}}. \tag{12}$$

To capture failure due to out-of-plane loadings (e. g. peel stresses), an out-of-plane failure index F_{op} is defined by the following maximum stress failure criterion,

$$F_{\mathrm{op}} = \sqrt{\frac{\sigma_3^2}{X_z^2} + \frac{\tau_{13}^2}{S_z^2} + \frac{\tau_{23}^2}{S_z^2}}, \tag{13}$$

where X_z and S_z are the interlaminar tensile and shear strengths respectively.

The stress state in each UD discontinuous ply oriented at θ_i is known from equation 10. Therefore, combining quadratically the in-plane and out-of-plane failure indices, a global failure index $F_{\mathrm{I}}(\theta_i)$ for

the $N_{ply}(\theta_i)$ plies with orientation θ_i can be obtained

$$F_{\mathrm{I}}(\theta_i) = \sqrt{F^2_{\mathrm{ip}}(\theta_i) + F^2_{\mathrm{op}}(\theta_i)}. \tag{14}$$

A quadratic failure criterion was chosen due to the necessity of combining in a simple and effective way two failure indices in a single one. Note also that equation 14 is ultimately a sum of squares of ratios of stresses and strength. Such kind of quadratic criterion are indeed widely adopted to model the interaction of failure modes in composite laminate [33]. Nevertheless, for the purpose of failure within TBDCs, it was useful to keep the two in-plane and out-of-plane indices distinct, as it will be shown in section 4.

3.2.3. Stiffness reduction of the TBDC

Following a ply-discount method, it is assumed that a discontinuous ply with in-plane orientation θ_i fails and no longer carries any stress if the respective $F_{\mathrm{I}}(\theta_i) \geq 1$. This reduces the stiffness of the EL resulting from the stochastic orientation tensor. This stiffness reduction can be represented by a damage tensor $\mathbf{d}^{\mathrm{EL}}$ which can be computed by the ratio of the components of the damaged $\mathbf{C}_{\mathrm{EL,d}}$ and pristine $\mathbf{C}_{\mathrm{EL,p}}$ stiffness tensors of the EL [34]. Given the stacking sequence of an EL (as defined in Section 3.2.1), the corresponding stiffness tensor $\mathbf{C}_{\mathrm{EL}}$ can be obtained using the extensional component (i.e. "A" matrix only) of the Classical Laminate Theory (CLT):

$$\mathbf{C}_{\mathrm{EL}} = \sum_{i=1}^{N_\theta} \mathbf{C}^i_{\mathrm{D},\theta_i} \cdot r_{\theta_i} \tag{15}$$

where $\mathbf{C}_{\mathrm{D},\theta_i}$ is the stiffness tensor of the UD discontinuous ply (see Appendix B) rotated by the respective in-plane angle θ_i.

The pristine stiffness tensor $\mathbf{C}_{\mathrm{EL,p}}$ is calculated with equation 15 using the original FOD $\mathcal{F}^{\mathrm{EL}}(\theta, \frac{\pi}{2})$. The probability r_{θ_i} of the plies oriented at θ_i with $\mathcal{F}_{\mathrm{I}}(\theta_i) \geq 1$ is set to 0, and equation 15 is used to compute the damaged stiffness tensor $\mathbf{C}_{\mathrm{EL,d}}$. Note that, if an infinite number of plies N_θ were considered for the EL, $\mathbf{C}_{\mathrm{EL,p}}$ would be equivalent to $\mathbf{C}^{\mathrm{g}}_{\mathrm{TBDC}}$, namely the stiffness tensor obtained with the orientation averaging scheme described in Section 3.1.3.

For the same applied strain, the surviving plies need to withstand the stress previously carried by the failed plies; therefore, following an iso-stress approach, $C_{\mathrm{EL,d}}$ is used to compute a local strain increase resulting from the stiffness loss of the EL (due to failure of the plies). This new strain is applied to the damaged EL, and CLT is used to recalculate the stress redistribution to the surviving plies. If this stress redistribution triggers the failure of new plies, the stiffness tensor is updated again, until the damaged EL is able to withstand the stress redistribution or it fails completely.

Following the approach presented in [34], the direct components of both $C_{\mathrm{EL,p}}$ and $C_{\mathrm{EL,d}}$ are used to calculate a damage tensor $\mathbf{d}^{\mathrm{EL}}$ as:

$$\mathbf{d}^{\mathrm{EL}} = \begin{bmatrix} D_{11} & 0 & 0 \\ 0 & D_{22} & 0 \\ 0 & 0 & D_{33} \end{bmatrix}, \qquad \text{with} \qquad D_{ii} = 1 - \frac{C_{\mathrm{EL,d},ii}}{C_{\mathrm{EL,p},ii}} \tag{16}$$

The damage tensor $\mathbf{d}^{\mathrm{EL}}$, calculated in equation 16 for the stiffness tensor $\mathbf{C}_{\mathrm{EL,p}}$ of the EL, can thus be applied to the stiffness tensor $\mathbf{C}^{\mathrm{g}}_{\mathrm{TBDC}}$, obtained via orientation averaging (see Section 3.1.3). However, this requires rotating $\mathbf{C}^{\mathrm{g}}_{\mathrm{TBDC}}$ from CSYS$^{\mathrm{g}}$ to CSYS$^{\mathrm{EL}}$. By doing so, the damaged stiffness tensor $\mathbf{C}^{\mathrm{EL}}_{\mathrm{TBDC,d}}$ is obtained as [34]:

$$\mathbf{C}^{\mathrm{EL}}_{\mathrm{TBDC,d}} = \begin{bmatrix} d_{\mathrm{L}}^2 C^{\mathrm{EL}}_{11,\mathrm{TBDC}} & d_{\mathrm{L}} d_{\mathrm{T}} C^{\mathrm{EL}}_{12,\mathrm{TBDC}} & d_{\mathrm{L}} d_{\mathrm{Z}} C^{\mathrm{EL}}_{13,\mathrm{TBDC}} & 0 & 0 & 0 \\ & d_{\mathrm{T}}^2 C^{\mathrm{EL}}_{22,\mathrm{TBDC}} & d_{\mathrm{T}} d_{\mathrm{Z}} C^{\mathrm{EL}}_{23,\mathrm{TBDC}} & 0 & 0 & 0 \\ & & d_{\mathrm{Z}}^2 C^{\mathrm{EL}}_{33,\mathrm{TBDC}} & 0 & 0 & 0 \\ & & & d_{\mathrm{TZ}} C^{\mathrm{EL}}_{44,\mathrm{TBDC}} & 0 & 0 \\ & sym. & & & d_{\mathrm{ZL}} C^{\mathrm{EL}}_{55,\mathrm{TBDC}} & 0 \\ & & & & & d_{\mathrm{LT}} C^{\mathrm{EL,p}}_{66,\mathrm{TBDC}} \end{bmatrix} \tag{17}$$

where:

$$d_L = 1 - D_{11}, \qquad d_T = 1 - D_{22}, \qquad d_Z = 1 - D_{33},$$
$$d_{\mathrm{TZ}} = \left(\frac{2 d_{\mathrm{T}} d_{\mathrm{Z}}}{d_{\mathrm{T}} + d_{\mathrm{Z}}} \right)^2, \qquad d_{\mathrm{ZL}} = \left(\frac{2 d_{\mathrm{Z}} d_{\mathrm{L}}}{d_{\mathrm{Z}} + d_{\mathrm{L}}} \right)^2, \qquad d_{\mathrm{LT}} = \left(\frac{2 d_{\mathrm{L}} d_{\mathrm{T}}}{d_{\mathrm{L}} + d_{\mathrm{T}}} \right)^2 \tag{18}$$

The damaged stiffness tensor $\mathbf{C}^{\mathrm{EL}}_{\mathrm{TBDC,d}}$ is then rotated back to CSYS$^{\mathrm{g}}$, where the new global stress state is calculated.

The implementation of the material model used in the proposed stochastic FE framework was done via a UMAT, and is summarised in Figure 8.

4. Results

The proposed stochastic FE framework is validated against experimental tensile tests of the two materials presented in Section 2. The results of the stochastic FE framework are also compared to a deterministic FE approach, in which the fibre orientation tensors that result from a process simulation are directly mapped to the FE structural mesh (as shown in Figure 2), with no stochastic

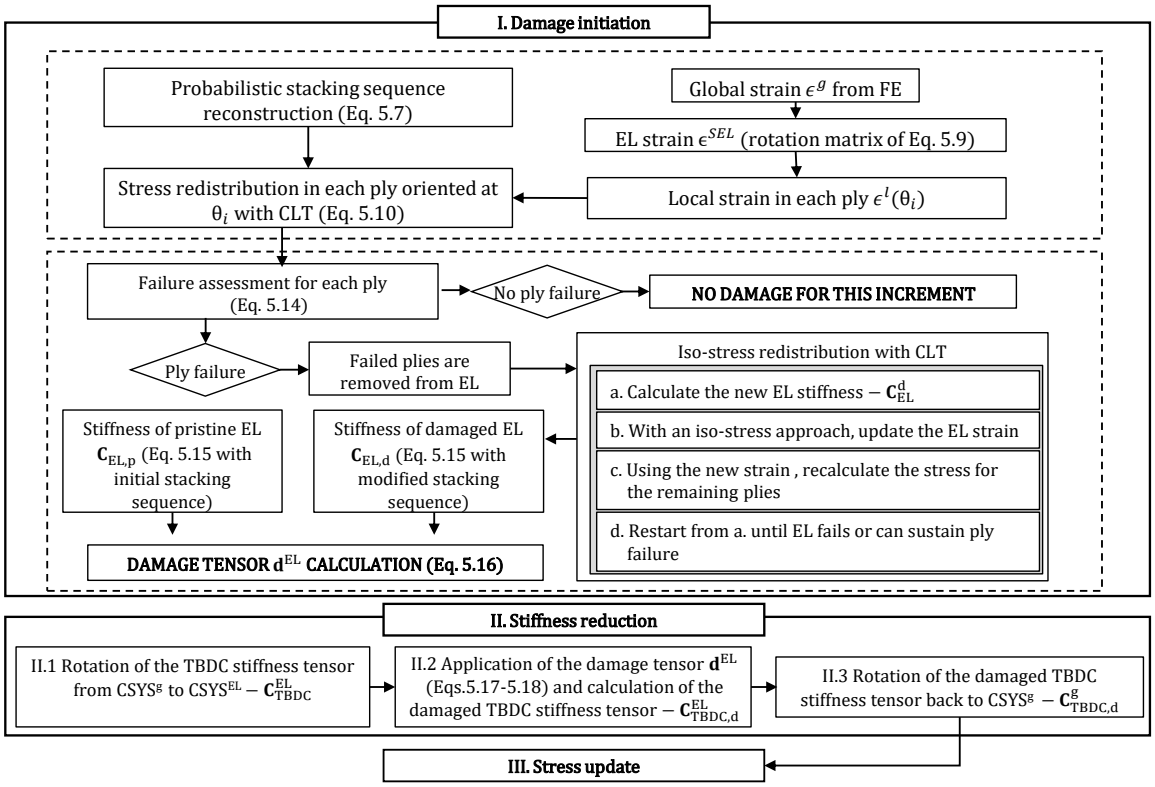

Figure 8: Implementation flowchart of the UMAT used in the stochastic FE framework.

process involved. The material properties used as inputs are summarised in Table 2, and the specimen geometries and numerical inputs are summarised in Table 3. For all simulations, full integration linear brick elements (C3D8) were used. One element was used through the thickness, while the in-plane dimensions are reported case-by-case.

TABLE 2: Tow material properties used as model inputs. Modulus values are in GPa, strength values are in MPa, toughness values are in kJ/m^2.

Material	E_1^{t}	E_2	G_{12}	ν_{12}	$X_{\mathrm{T}}^{\mathrm{t}}$	Y_{T}	Y_{C}	S	X_z	S_z	$\mathcal{G}_{\mathrm{int}}^{\mathrm{IIc}}$
HexPly-M77 [35]	129†	9.0*	5.6*	0.34*	1258†	73*	200*	78*	73*	78*	0.8†
CF-SMC tows [36]	98	5.6	2.1	0.34	895	35	180	40	35	40	1.0*

† Values taken from uni-axial tensile tests of the UD material system, and linearly scaled to the fibre content of the respective TBDC material system.

* Estimated values based on the literature [37].

TABLE 3: Specification of the geometry and number of the tested specimens and of the numerical inputs.

Material	l^{s} (mm)	w^{s} (mm)	t^{s} (mm)	N^{t}	$\Delta\theta$ (°)
HexMc M77†	138	50	3.0	24	10
CF-SMC‡	150	25	2.5	15	10

† 10 specimens were tested for HexMC-M77.

‡ 6 specimens were tested for the 0°, 45° and 90° CF-SMC configurations.

4.1. Sensitivity to the mesh size and to numerical input parameters

Figures 9a and 9b show the influence of the mesh size used in the stochastic FE simulations, on the predicted stress-strain response and ultimate strength. For this analysis, the same specimen generated with the stochastic FE framework was discretised into different element sizes (for the structural mesh). For the smallest element size (0.5 mm), the load drop after failure of the virtual specimen was captured. This was no longer true for increasing element sizes, due to numerical convergence issues close to final failure. Therefore, for the remaining results of the FE simulations presented in this paper, an element size of 0.5 mm was used.

The in-plane angle spacing $\Delta\theta$ was introduced as numerical parameter in the construction of the EL (Section 3.2.1). Using the HexMC-M77 simulations, Figure 9c shows that the variation of the angle spacing $\Delta\theta$ has small effects on the model accuracy, with no more than 10% maximum discrepancy between the lowest and highest predicted strengths. Such low sensitivity is mainly due to the fact that the model predicts failure in the elements with higher strain, but in the plies oriented at the closest angle to 0°. A 60° discretisation allows for three orientations exclusively, namely 30°, 90° and 120°. Therefore, the largest variation of θ is only of about 30°, which likely explains the reduced sensitivity on this parameter.

Figure 9d shows that the computation time required increases exponentially for finer angle discretisations. For all the FE simulations a value of $\Delta\theta = 10°$ was used, as it was considered the best compromise between accuracy and computational efficiency.

4.2. Analysis and characterisation of the strain variability

The variability of the strain fields obtained with the deterministic and stochastic FE models are here compared to the variability of strain fields measured with DIC from HexMC-M77 specimens [13]. Figure 10a compares the predicted strain distribution to the one measured with DIC. It is found that the deterministic approach is not able to capture the correct strain distribution, showing a significantly smaller variablity and underpredicting the maximum strain by about 32%. Conversely, the stochastic approach recreates a similar strain distribution to that measured with DIC, with a more similar strain variability and only 8% maximum strain underprediction. Such discrepancy is likely due to non-considered feature like resin pockets or tow ends.

The spatial length-scales of the strain fields are compared in Figure 10b, using the method based on the triangulation of peaks and troughs, proposed in [13]. Once again, the deterministic FE approach fails to predict the spatial features of the strain fields, having a characteristic length scale ($\bar{s}_{\mathrm{ls}}$) significantly smaller than that of the DIC strain fields. However, due to the spatial distribution of the seed points used to generate the stohastic FE models, the characteristic length scale of the resulting strain fields is in good agreement with that of the DIC strain fileds.

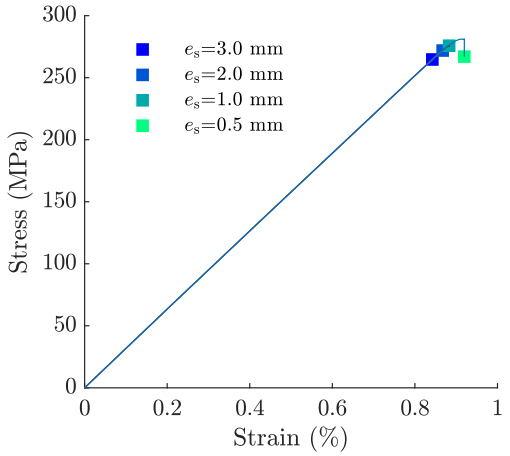

(a) Predicted stress-strain responses for different mesh sizes.

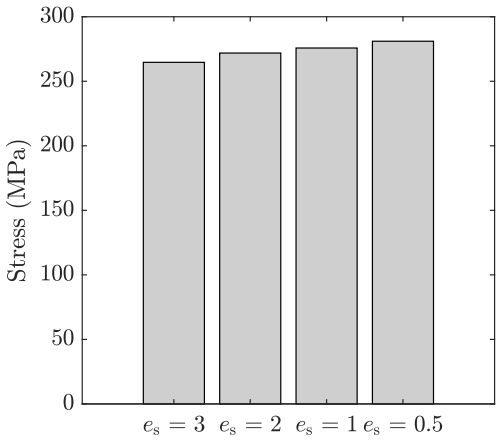

(b) Ultimate strength predicted for different mesh sizes.

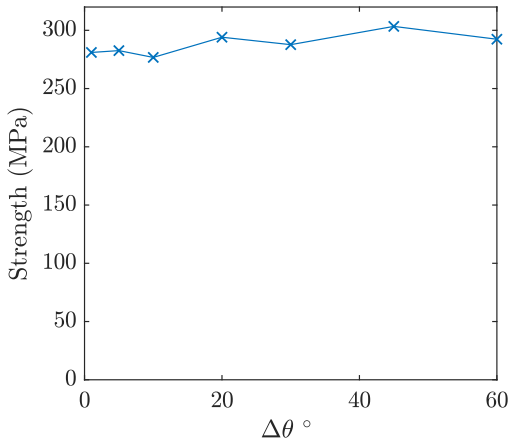

(c) Effect of $\Delta\theta$ on the predicted ultimate strength.

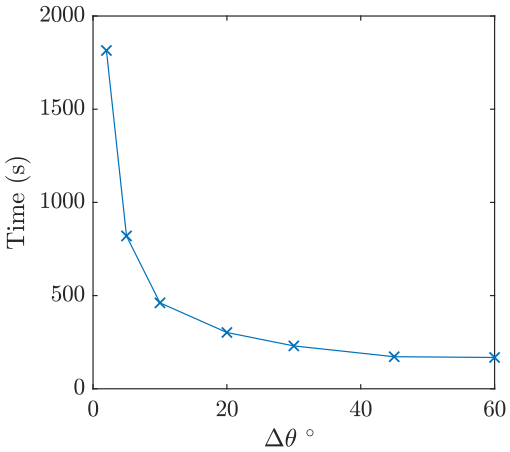

(d) Effect of $\Delta\theta$ on the simulation time.

Figure 9: Effects of numerical parameters on the predictions and efficiency of the framework for a given HexMC-M77 virtual specimen.

Figure 11 compares fields of different properties of a virtually generated specimen with the stochastic FE approach. It is shown that the field of failure indices (F_{I}), shown in Figure 11a, strongly depends on the longitudinal strain ϵ_X (Figure 11b), which in turn is correlated with the field of $\bar{a}^g_{XX}$ (Figure 11c), where regions dominated by transverse fibre orientations present higher strains. The model thus captures correctly the TBDCs tendency to fail in high strain regions, as it was experimentally demonstrated by DIC investigations reported in the literature [24, 38, 39]. In contrast, the longitudinal stress field σ_X (Figure 11d) is not significantly correlated to the F_{I} field. Moreover, Figures 11e and 11f show the contribution of the in-plane and out-of-plane failure indices to the overall failure index F_{I}; as expected for the specimen geometry, the in-plane failure has the most dominate contribution to the failure prediction. This analysis demonstrates the importance of capturing the accurate variability of the field material properties to predict the mechanical response of TBDC material system.

Figure 12a shows the statistical distribution of the stochastic term $\bar{a}_{XX}$(taken from all seed points

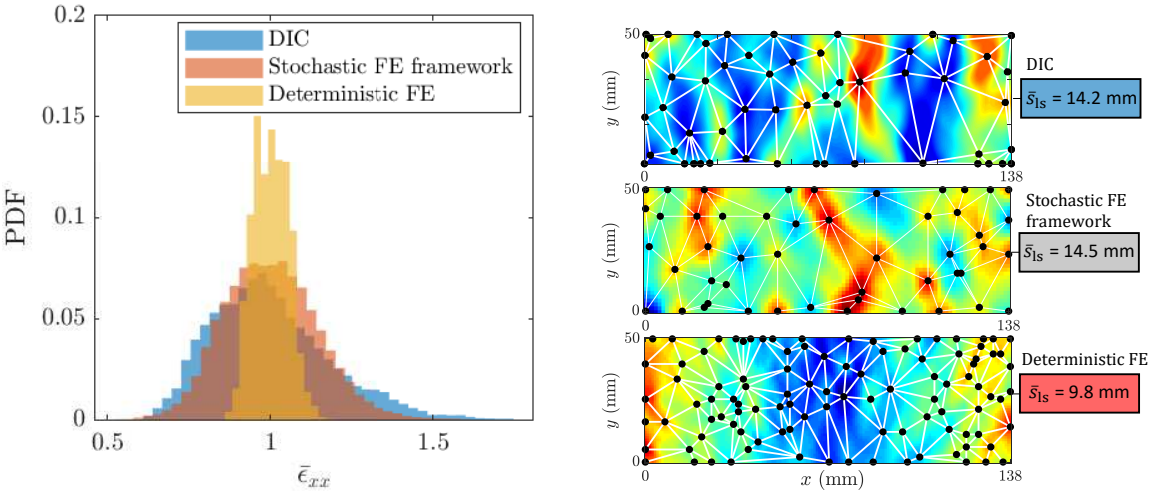

(a) Distribution of the normalised strain values.

(b) Representation of the characteristic length scales.

Figure 10: Analysis of the variability of the FE (deterministic and stochastic) and DIC strain fields for the HexMC-M77 material. Note that the coloured plots in (b) have the same colour range (for visibility purposes) but different strain ranges, as shown in (a).

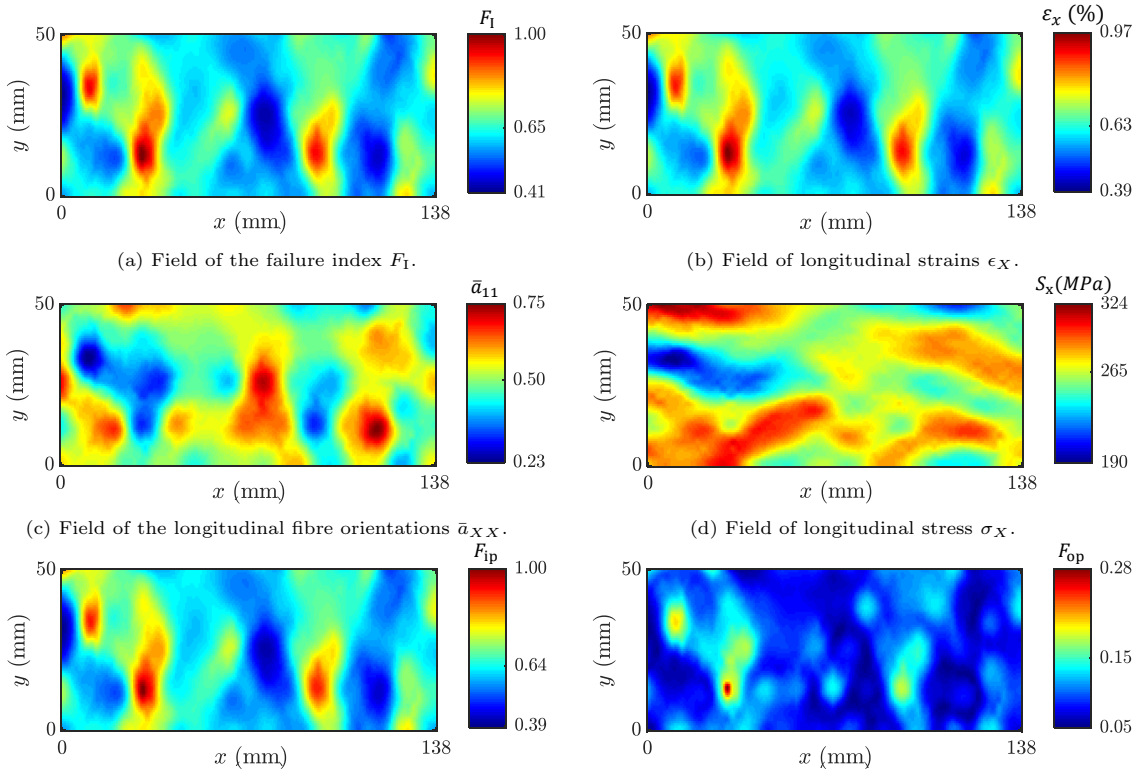

(a) Field of the failure index F_{I}.

(b) Field of longitudinal strains ϵ_X.

(c) Field of the longitudinal fibre orientations $\bar{a}_{XX}$.

(d) Field of longitudinal stress σ_X.

(e) Field of the in-plane failure index F_{ip}.

(f) Field of the out-of-plane failure index F_{op}.

Figure 11: Fields of outputs obtained with the stochastic FE framework for a HexMC-M77 specimen..

of a virtual specimen) as a function of N^{t} for the HexMC-M77 specimens. Due to the uniformly random in-plane orientation of the tows in this case, the average value of $\bar{a}_{XX}$ is expected to be very close to 0.5. For values of $N_{\mathrm{t}} \leq 20$ there is a large scatter of $\bar{a}_{XX}$ values, with the lower values defining to regions with dominant transverse fibre orientations (relative to the loading direction), and hence

corresponding to weaker regions within the specimen. Figure 12b shows the resulting influence of N^{t} on the predicted average strength and standard deviation of 10 virtual specimens. It is shown that lower values of N^{t} lead to lower average predicted strength values with a higher standard deviation, and higher N^{t} values lead to higher strength values with a narrower standard deviation (for the TBDC material analysed in this Figure, $N^{\mathrm{t}} = 24$).

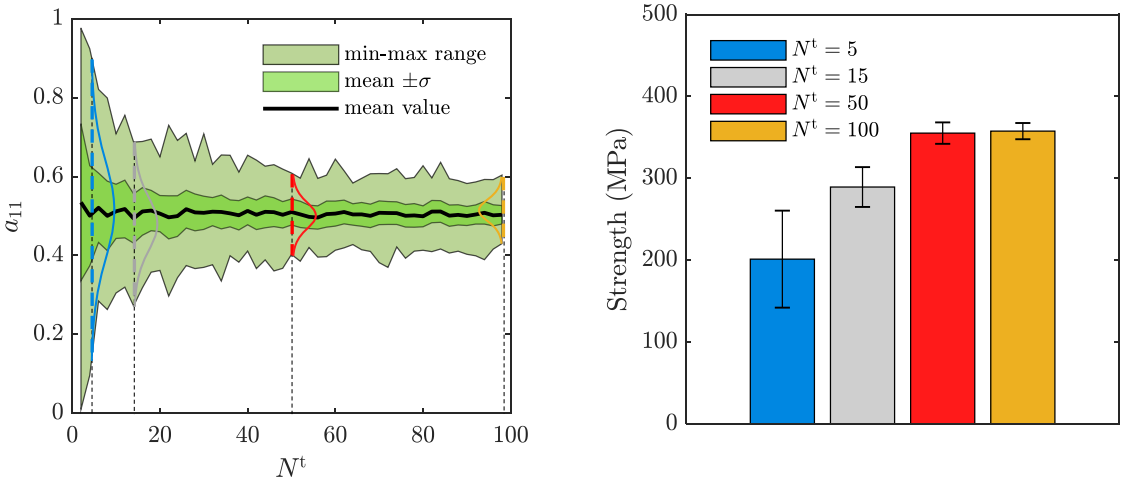

(a) Convergence of $\bar{a}_{XX}$ with N^{t}.

(b) Effect of N^{t} on predicted ultimate strength.

Figure 12: Influence of N_{t} on the predictions of the stochastic FE framework for the HexMC-M77 material system. In this figure, σ represents one standard deviation

Finally, note that in this work N_t is considered as the through-the-thickness tow count, and one element through the thickness was used. For more complex simulations, where more elements may be considered through the thickness, it may be required to consider N_t as the number of tows along the element size (since TBDCs are generally used for thin components).

4.3. Results of the FE framework and validation against experiments

In this Section, the results of the stochastic framework are compared to the experimental tensile tests of the two materials described in Section 2 and to the results obtained with a deterministic FE approach. For each material system tested, a process simulation of a plate was performed (see Appendix A for more details). For the deterministic FE approach, the fibre orientation tensors were directly mapped to an FE mesh (with the respective specimen geometry, specified in Table 3); in the formulation described in Section 3, this is equivalent to setting $\bar{\mathbf{a}} = \mathbf{a}$. For the stochastic FE approach, the orientation tensors were mapped to the seed points of the FE mesh (with the same specimen geometry). Therefore, only one simulation is performed for the deterministic approach, and the number of simulations performed with the stochastic approach was the same as the number of specimens tested.

In Figure 13, the results predicted with both the deterministic and stochastic FE approaches are compared to the experimental results of the CF-SMC specimens with different preferential fibre

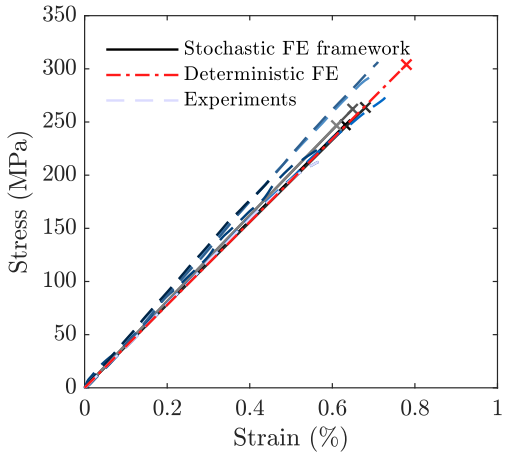

(a) Predicted and experimental stress strain curves for the 0° CF-SMC specimens.

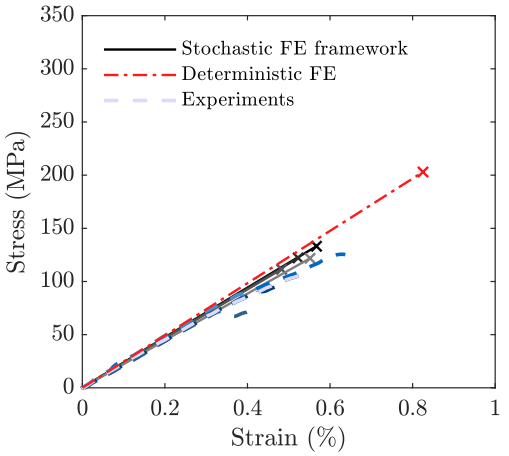

(b) Predicted and experimental stress strain curves for the 45° CF-SMC specimens.

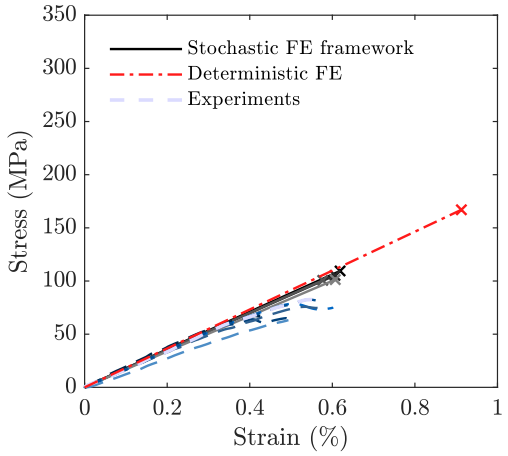

(c) Predicted and experimental stress strain curves for the 90° CF-SMC specimens.

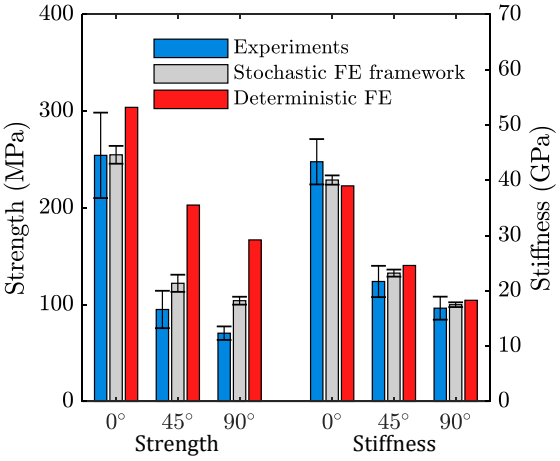

(d) Predicted and experimental strength and stiffness for all the CF-SMC specimens

Figure 13: Validation of the stochastic FE framework against the experimental results of the CF-SMC.

orientations. The strength and stiffness predictions of the stochastic FE approach are in good agreement with the experimental results, whereas the deterministic FE approach, despite being able to predict accurate stiffness values, over-predicts the strength, in particular for the 45° and 90° specimens.

The predictions of both FE approaches are compared to the experimental results of the HexMC-M77 specimens (with $t^{\mathrm{t}} = 0.125$ mm) in Figures 14a and 14b. Once again it is shown that the lack of variability in mechanical properties of the deterministic approach leads to over-predictions of the specimens' mechanical properties. On the other hand, the realistic variability included in the stochastic FE approach leads to more accurate predictions. The same HexMC-M77 material system but with a tow thickness of $t^{\mathrm{t}} = 0.285$ mm has been tested and reported in the literature [17]. In Figure 14c, the strength and stiffness predictions with both FE approaches are compared to the experimental results reported in [17], where once again good predictions are obtained with the stochastic FE approach.

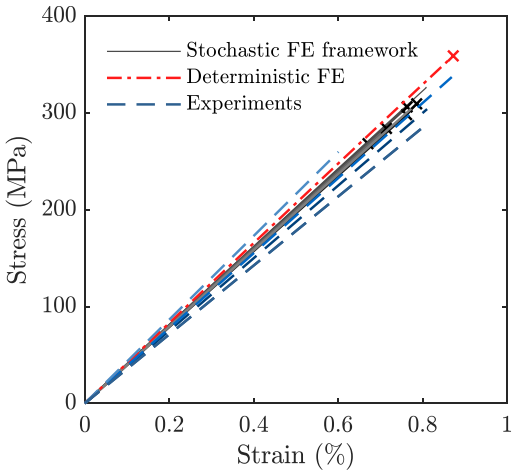

(a) Predicted and experimental stress strain curves for the HexMC-M77 ($t^t = 0.164$ mm).

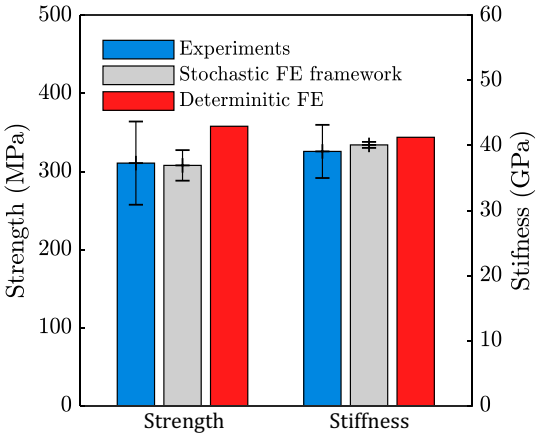

(b) Predicted and experimental strength and stiffness for the HexMC-M77 ($t^t = 0.125$ mm).

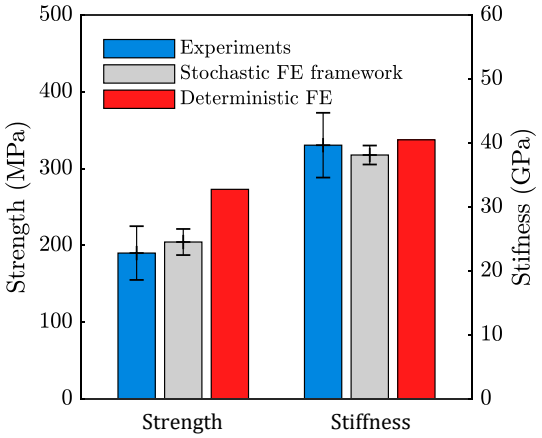

(c) Predicted and experimental strength and stiffness for the HexMC-M77 ($t^t = 0.285$ mm) [17].

Figure 14: Validation of the stochastic FE framework against the experimental results of the HexMC-M77.

5. Discussion

5.1. Reproducing the stochastic nature of TBDCs and the problem with a deterministic approach

The implicit description of the material's microstructure, in the deterministic FE approach, is directly linked to the local orientations tensors that result from process simulations. It was shown in Figure 10b that the spatial length-scales in the strain fields predicted by this approach do not reflect the characteristic length-scales of the material's microstructure (which is dependent on the tow geometry). Moreover, the quantitative strain variability of the deterministic FE approach is significantly lower than that of the DIC strain fields. For this reason, and since failure of the material is associated to local strain peaks [24], as shown in Figure 11, the deterministic approach constantly over-predicts the strength of these materials.

The stochastic framework is able to capture more realistic strain peaks (which correspond to areas with tows more aligned in the transverse direction to the load); this is the consequence of the random sampling of orientations from the planar FODs, with the number of samples equal to the average

tow count N^{t} along the thickness of the specimens. The influence of N^{t} on the predicted strength is shown in Figure 12b, where it was shown that higher average strength values result from a higher tow count, which reduces the probability of local weak spots in the material that trigger premature failure, as shown in Figure 12a. This is in agreement with what has been reported in the literature [18, 40], on the effect of the specimen thickness on the material strength.

The stochastic FE approach, while achieving significantly better results than the deterministic FE one, still tends to show some strength overpredictions (see Figure 13d and Figure 14c). This is likely due to the aforementioned maximum strain underprediction (see Figure 10a). Including the local effects of resin pockets and tow ends in the model might improve its predictive capabilities of both the maximum strain and the resulting strength in the simulated material. It is also suggested that a more complete description of the TBDCs' microstructure may lead to a better prediction of the strengths' scatter, which currently is underpredicted (see Figure 13d and Figure 14c). Currently, the main microstructural features leading to failure are unfavourably oriented tows. Considering the stochastic presence and location of resin pockets and tow ends may extend the range of microstructural features causing failure. As a result, strength variability may increase. But significantly more work is required to confirm such hypotheses.

The stiffness predictions of both FE approaches are very similar and both are in good agreement with the experimental results. This is due to the fact that stiffness is mainly governed by the average fibre orientation state, rather then local features in the microstructure, and therefore the inherent local material variability does not play a significant role in the average stiffness. This shows that despite process simulations not being able to capture local material variability, they are able to predict the average fibre orientation state in a specimen. Moreover, in the stochastic FE approach, the orientation tensors that are mapped to the seed points (from the process simulation) and converted to stochastic orientation tensors, still preserve the original average orientation state; this was confirmed by the accurate stiffness predictions obtained.

5.2. Novelty and potential impact

The stochastic FE framework presented in this work is able to include fibre orientation tensors (that results from process simulations) in structural FE simulations, while still being able to reproduce the intrinsic variability of TBDC material systems. Linking process and structural simulations is a common practice both in the literature [19, 21, 41] and in proposed commercial software [10]; these approaches, however, rely directly on the process simulation predictions to reproduce the material variability. As a result, these works often propose a novel, more accurate process simulation, like explicit modelling of the tows [19, 41]. The approach proposed in this work does not rely on the accurate predictions of a process simulation, but rather solves the problem introducing an additional

probabilistic step to model the material's intrinsic stochasticity, which is likely a more efficient and scalable approach.

A failure criterion is used in combination with a ply discount method to predict final failure of an EL associated to a TBDC. The implementation of the FE framework offers the efficiency and flexibility to model different geometries, and perform Monte Carlo analysis to obtain the stochastic dominated response. Moreover, enabling the link between structural simulations and the manufacturing process can allow for the evaluation and optimisation of the charge patterns (used in the compression moulding process) that maximise the performance of a specific component; this can help engineers to manufacture more efficient and reliable TBDC structures and which comply with specific design allowables.

Capturing the variability in material systems with heterogeneous microstructures is essential to predict their mechanical properties. The applicability of this framework can also be extended to other material systems with such an heterogeneous microstructure; the modular implementation of the framework allows for the use of other material models (suitable for a particular material systems), enabling its use to model/predict the mechanical properties of a wider range of materials.

The efficiency and versatility of the approach is also due to an implicit representation of the microstructure. This is significantly more efficient and scalable than an explicit tow modelling, regrdless if this is done in the process simulation [19, 41] or in the structural analysis [5, 6, 18, 42, 43]. Other works have proposed an implicit representation of the microstructure [12, 44], but not linked with a process simulation. Therefore, these approaches are mainly applicable to low-flow randomly oriented TBDCs and with no geometrical complexities, like ribs or corners, that might locally reorient some tows.

6. Conclusions

This work presents a FE framework to model the stochastic behaviour of TBDC material systems. Fibre orientation tensors resulting from flow simulations are integrated in the framework, and a failure criterion for an equivalent discontinuous ply is presented and combined with a ply-discount method to predict final failure. The main conclusions of this work are as follows:

- Using fibre orientations resulting from process simulations in a deterministic FE approach leads to inaccurate field of mechanical properties, both in terms of their quantitative variability and characteristic length-scales.

- Integrating the results from process simulations in the stochastic FE framework leads to accurate and representative field of mechanical properties, while still preserving the overall orientation state obtained with the process simulations.

- The framework was validated against experimental results of specimens of two different material systems loaded under tension: the HexMC-M77 (low flow) and a CF-SMC (with high flow, and three different preferential fibre orientations). The FE framework yielded accurate results, and was able to replicate the strain variability and the resulting strength of these materials.
- The proposed 3D model showed the flexibility to couple flow simulations and FE structural simulations including failure progression in a stochastic process that assigns the realistic intrinsic material variability of the material system. The implicit representation of the microstructure of the material allows the framework to be used in an efficient way (compared to models with explicit representations of the microstructure), and has the potential to be scaled to larger and more complex models.

Acknowledgments

The research leading to these results has been performed within the framework of the FiBreMoD project and has received funding from the European Union's Horizon 2020 research and innovation programme under the Marie Skłodowska-Curie grant agreement No 722626. SVL holds the Toray Chair for composite materials at KU Leuven, the support of which is gratefully acknowledged. SP acknowledges her Research Fellowship of the Royal Academy of Engineering on "Multiscale discontinuous composites for high-volume and sustainable applications" (2015-2019). YS acknowledges FWO Flanders for his postdoctoral fellowship. The authors also acknowledge Mitsubishi Chemical Carbon Fiber and Composites GmbH for providing material and related information. The authors acknowledge Stefan K. Nothdurfter and Karsten Schuffenhauer from the Department of Advanced Composites and Lightweight Structures Development of Automobili Lamborghini S.p.A. for providing the HexMC-M77 plates used for experimental validation, and for many insightful discussions. The authors are also thankful to Tahreem Naveed for helping obtaining the experimental data shown for the HexMC-M77 material.

Appendix A Process simulation of plates and fibre orientation mapping to the specimen mesh

Compression moulding simulations for both HexMC and CF-SMC plates were performed, as first step of the modular framework. The software used is Moldex3D, which implements a dedicated compression moulding tool and an improved Anisotropic Rotary Diffusion model (iARD) for the fibre orientation predictions [45]. Walls are considered as rigid boundaries. A 1 mm mesh size was considered, using the automated solid mesh generator implemented in Moldex 3D. This was judged

sufficient, since the simulated geometry is very simple and no shell-core layered microstructure was expected, as it is the case of injection moulded materials. Its parameters were calibrated to reproduce the average orientation tensor measured in the CF-SMC specimens, as explained in [24]. The calibrated parameters obtained in this way are presented in Table 4. The same parameters are also used for the HexMC plate simulation. A planar random fibre orientation was set for the charges. Figure 15 shows the results of both simulations. The image also shows the initial location and shape of the charges and the mapping locations of the specimens. As shown, a certain range of a_{XX} is present, but the extreme values are either located in the proximity of the walls (like the values a_{XX} smaller than 0.4 in the SMC simulation, see Figure 15b), or are smaller local variations respect to the global predicted orientation. This variation is not thus caused by the intrinsic variability of the TBDCs, but rather to edge or numerical effects. The location of extraction of the virtual specimens was thus selected to make these effects negligible (for example, the HexMC specimen was extracted from a central location, with little variation of a_{XX}, see 15a). Overall, as reported in [24], the simulation software was capable of capturing correctly the global average orientation measured in the specimens while, as it was showed in this work, it failed to capture the intrinsic tow orientation variability. This lack of accuracy justifies the creation of the proposed framework.

TABLE 4: The calibrated parameters of the iARD model, used for the process simulation.

C_I	C_M	α
0.03	0.9	0.7

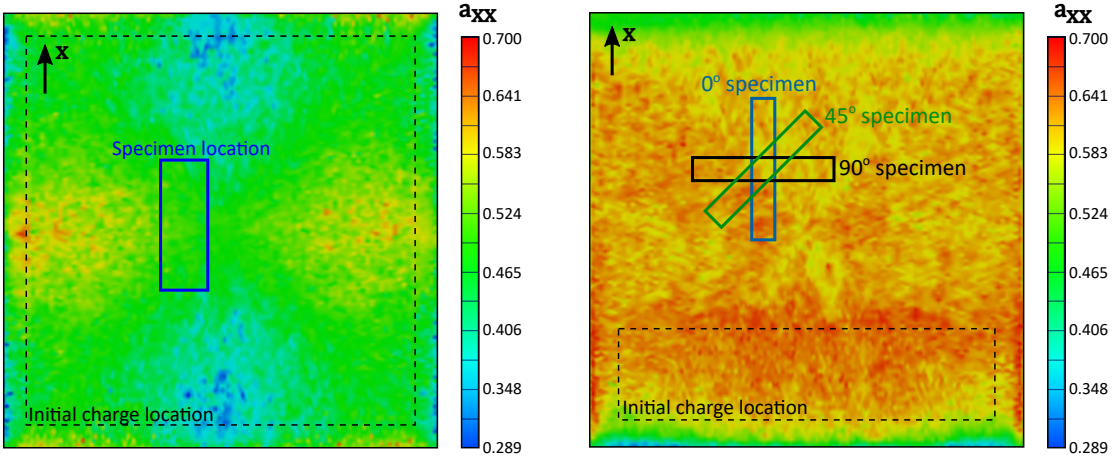

(a) Low-flow compression moulding simulation of the HexMC-M77 material.

(b) High-flow compression moulding simulation of the CF-SMC material.

Figure 15: Fields of the a_{XX} component (surface values)
of the orientation tensors resulting from the process simulations. The location of the orientations mapped to the specimen meshes is highlighted in each subfigure.

Finally, note that the adopted approach is based on the compression moulding simulation of an homogenised materials. Other approaches proposed in the literature simulate explicitly the tows and

the matrix [19, 46, 47]. While these may achieve a better accuracy, for the purpose of the present work, a commercially available tool was necessary.

Appendix B Stiffness tensor of a UD discontinuous ply

$$E_1^{\mathrm{t}} = \frac{E_1^{\mathrm{UD}}}{1 + \frac{1}{\lambda_i \cdot l_{\mathrm{char}} \cdot \tanh(\lambda l_{\mathrm{char}})}} \cdot V_{\mathrm{t}}^{\mathrm{TBDC}}, \quad \text{with} \quad \lambda = \sqrt{2G_{12}^{\mathrm{UD}}/(t_{\mathrm{char}} \cdot t^{\mathrm{m}} \cdot E_1^{\mathrm{UD}})}, \tag{B.1}$$

where E_1^{UD} is the longitudinal Young's modulus of the UD material from which the tows are made, and G_{12}^{UD} is the in-plane shear modulus. The shear-lag characteristic dimensions of the tows are $l_{\mathrm{char}} = l^{\mathrm{t}}/8$ and $t_{\mathrm{char}} = w^{\mathrm{t}} \cdot t^{\mathrm{t}}/[2(w^{\mathrm{t}} + t^{\mathrm{t}})]$[48, 49], where t^{t} and w^{t} are the tow thickness and width, respectively. Assuming a square packing of the fibres and neglecting resin-rich regions between the tows, the average matrix thickness surrounding a tow is given by the interfibre distance $t^{\mathrm{m}} = (\sqrt{\pi/(4V^{\mathrm{f}})} - 1) \cdot \phi_{\mathrm{f}}$, where ϕ_{f} is the fibre diameter, and V^{f} is fibre volume fraction.

The equivalent transverse elastic properties of a tow are derived from the Halpin-Tsai general expression [33] for a property P in direction b (where the superscripts "t", "m", "UD" correspond to the discontinuous tow, matrix and discontinuous uni-directional composite, respectively):

$$P_b^{\mathrm{t}} = P^{\mathrm{m}} \frac{1 + \eta_b \xi_b V_{\mathrm{t}}^{\mathrm{TBDC}}}{1 - \eta_b V_{\mathrm{t}}^{\mathrm{TBDC}}}, \quad \text{with} \quad \eta_b = \frac{\frac{P_b^{\mathrm{UD}}}{P^{\mathrm{m}}} - 1}{\frac{P_b^{\mathrm{UD}}}{P^{\mathrm{m}}} + \xi_b}, \tag{B.2}$$

with $V_{\mathrm{t}}^{\mathrm{TBDC}}$ representing the volume fraction of tows in the TBDC; in this work a value of $V_{\mathrm{t}}^{\mathrm{TBDC}} = 1$ was assumed.

The Halpin-Tsai geometric coefficients are $\xi_{22} = 2(w^{\mathrm{t}}/t^{\mathrm{t}})$, $\xi_{33} = 2(t^{\mathrm{t}}/w^{\mathrm{t}})$ and $\xi_{12} = \xi_{13} = \xi_{23} = 1$, assuming tows with a rectangular cross-section [50] and a transverse isotropic behaviour. The equivalent stiffness tensor of a discontinuous ply $\mathbf{C}_{\mathrm{D}}$ can therefore be defined as,

$$\mathbf{C}_{\mathrm{D}} = {\mathbf{S}_{\mathrm{D}}}^{-1} = \begin{bmatrix} \frac{1}{E_1^{\mathrm{t}}} & -\frac{\nu_{21}^{\mathrm{t}}}{E_2^{\mathrm{t}}} & -\frac{\nu_{31}^{\mathrm{t}}}{E_3^{\mathrm{t}}} & 0 & 0 & 0 \\ -\frac{\nu_{12}^{\mathrm{t}}}{E_1^{\mathrm{t}}} & \frac{1}{E_2^{\mathrm{t}}} & -\frac{\nu_{32}^{\mathrm{t}}}{E_3^{\mathrm{t}}} & 0 & 0 & 0 \\ -\frac{\nu_{13}^{\mathrm{t}}}{E_1^{\mathrm{t}}} & -\frac{\nu_{23}^{\mathrm{t}}}{E_2^{\mathrm{t}}} & \frac{1}{E_3^{\mathrm{t}}} & 0 & 0 & 0 \\ 0 & 0 & 0 & \frac{1}{G_{23}^{\mathrm{t}}} & 0 & 0 \\ 0 & 0 & 0 & 0 & \frac{1}{G_{13}^{\mathrm{t}}} & 0 \\ 0 & 0 & 0 & 0 & 0 & \frac{1}{G_{12}^{\mathrm{t}}} \end{bmatrix}^{-1}. \tag{B.3}$$

References

[1] L. Harper, D. Burn, M. Johnson, and N. Warrior, "Long discontinuous carbon fibre/polypropylene composites for high volume structural applications," *Journal of Composite Materials*, vol. 52, no. 9, pp. 1155–1170, 2018.

[2] M. Selezneva, K. Kouwonou, L. Lessard, and P. Hubert, "Mechanical properties of randomly oriented strand thermoplastic composites," *19th International Comittee on Composite Materials*, pp. 480–488, 2015.

[3] S. Pimenta, A. Ahuja, and A. Yong, "Damage tolerant tow-based discontinuous composites," in *ICCM20, Copenhagen, Denmark*, July 2015.

[4] Y. Wan and J. Takahashi, "Tensile and compressive properties of chopped carbon fiber tapes reinforced thermoplastics with different fiber lengths and molding pressures," *Composites Part A: Applied Science and Manufacturing*, vol. 87, no. August, pp. 271–281, 2016.

[5] Z. Chen, H. Tang, Y. Shao, Q. Sun, G. Zhou, Y. Li, H. Xu, D. Zeng, and X. Su, "Failure of chopped carbon fiber Sheet Molding Compound (SMC) composites under uniaxial tensile loading: Computational prediction and experimental analysis," *Composites Part A: Applied Science and Manufacturing*, vol. 118, no. December 2018, pp. 117–130, 2019.

[6] L. Harper, C. Qian, R. Luchoo, and N. Warrior, "3D geometric modelling of discontinuous fibre composites using a force-directed algorithm," *Journal of Composite Materials*, vol. 51, pp. 2389–2406, jul 2017.

[7] Y. Li, Z. Chen, L. Su, W. Chen, X. Jin, and H. Xu, "Stochastic reconstruction and microstructure modeling of SMC chopped fiber composites," *Composite Structures*, vol. 200, no. May, pp. 153–164, 2018.

[8] M. Alves and S. Pimenta, "The influence of 3d microstructural features on the elastic behaviour of tow-based discontinuous composites," *Composite Structures*, vol. 251, p. 112484, 2020.

[9] P. S. Stelzer, B. Plank, and Z. Major, "Mesostructural simulation of discontinuous prepreg platelet based carbon fibre sheet moulding compounds informed by x-ray computed tomography," *Nondestructive Testing and Evaluation*, vol. 35, no. 3, pp. 342–358, 2020.

[10] MSC Sfotware, "Digimat 2022 manual," 2022.

[11] P. Feraboli, T. Cleveland, P. Stickler, and J. Halpin, "Stochastic laminate analogy for simulating the variability in modulus of discontinuous composite materials," *Composites Part A: Applied Science and Manufacturing*, vol. 41, no. 4, pp. 557 – 570, 2010.

[12] M. Selezneva, S. Roy, S. Meldrum, L. Lessard, and A. Yousefpour, "Modelling of mechanical properties of randomly oriented strand thermoplastic composites," *Journal of Composite Materials*, vol. 51, pp. 831–845, mar 2017.

[13] M. Alves, Y. Li, and S. Pimenta, "Characterising and modeling the variability of mechanical properties in tow based discontinuous composites," *Under preparation.*

[14] Y. Li, S. Pimenta, J. Singgih, C. Ottenwelter, and S. Nothdurfter, "Understanding and Modelling Variability in Modulus and Strength of Tow-Based Discontinuous Composites," in *21st International Conference on Composite Materials*, no. August, (Xi'an), pp. 20–25, 2017.

[15] S. K. Nothdurfter, Y. Li, S. Pimenta, A. Composites, L. S. Development, and S. K. Campus, "Virtual Design of Car Components Manufactured With High-Performance Discontinuous Composites," in *ECCM 18*, no. June, pp. 24–28, 2018.

[16] Y. Li and S. Pimenta, "Development and assessment of modelling strategies to predict failure in tow-based discontinuous composites," *Composite Structures*, vol. 209, pp. 1005 – 1021, 2019.

[17] Y. Li, S. Pimenta, J. Singgih, S. Nothdurfter, and K. Schuffenhauer, "Experimental investigation of randomly-oriented tow-based discontinuous composites and their equivalent laminates," *Composites Part A: Applied Science and Manufacturing*, vol. 102, pp. 64–75, 2017.

[18] S. G. Kravchenko, D. E. Sommer, B. R. Denos, A. J. Favaloro, C. M. Tow, W. B. Avery, and R. B. Pipes, "Tensile properties of a stochastic prepreg platelet molded composite," *Composites Part A: Applied Science and Manufacturing*, vol. 124, p. 105507, 2019.

[19] D. E. Sommer, S. G. Kravchenko, B. R. Denos, A. J. Favaloro, and R. B. Pipes, "Integrative analysis for prediction of process-induced, orientation-dependent tensile properties in a stochastic prepreg platelet molded composite," *Composites Part A: Applied Science and Manufacturing*, vol. 130, p. 105759, 2020.

[20] A. J. Favaloro, D. E. Sommer, B. R. Denos, and R. B. Pipes, "Simulation of prepreg platelet compression molding: Method and orientation validation," *Journal of Rheology*, vol. 62, pp. 1443–1455, nov 2018.

[21] J. Görthofer, N. Meyer, T. D. Pallicity, L. Schöttl, A. Trauth, M. Schemmann, M. Hohberg, P. Pinter, P. Elsner, F. Henning, A. Hrymak, T. Seelig, K. Weidenmann, L. Kärger, and T. Böhlke, "Virtual process chain of sheet molding compound: Development, validation and perspectives," *Composites Part B: Engineering*, vol. 169, pp. 133–147, 2019.

[22] Hexcel, "HexMC User Guide." `https://www.hexcel.com/user_area/content_media/raw/HexMC_UserGuide.pdf`, 2014. [Online; accessed 04-April-2019].

[23] Mitsubishi Chemical Corporation, "Pyrofil STR120 datasheet." `https://www.m-chemical.co.jp/en/products/departments/mcc/molding-system/product/1212627_7526.html`. [Available on request].

[24] L. M. Martulli, L. Muyshondt, M. Kerschbaum, S. Pimenta, S. V. Lomov, and Y. Swolfs, "Carbon fibre sheet moulding compounds with high in-mould flow: Linking morphology to tensile and compressive properties," *Composites Part A: Applied Science and Manufacturing*, vol. 126, p. 105600, nov 2019.

[25] ASTM International, "ASTM D638-03 Standard Test Method for Tensile Properties of Plastics," West Conshohocken; PA, 2003.

[26] S. G. Advani and C. L. Tucker, "The use of tensors to describe and predict fiber orientation in short fiber composites," *Journal of Rheology*, vol. 31, no. 8, p. 751, 1987.

[27] M. Nachtane, F. Meraghni, G. Chatzigeorgiou, L. Harper, and F. Pelascini, "Multiscale viscoplastic modeling of recycled glass fiber-reinforced thermoplastic composites: Experimental and numerical investigations," *Composites Part B: Engineering*, vol. 242, p. 110087, 2022.

[28] A. D. Evans, C. C. Qian, T. A. Turner, L. T. Harper, and N. A. Warrior, "Flow characteristics of carbon fibre moulding compounds," *Composites Part A: Applied Science and Manufacturing*, vol. 90, pp. 1–12, 2016.

[29] Y. Wan, I. Straumit, J. Takahashi, and S. V. Lomov, "Micro-CT analysis of the orientation unevenness in randomly chopped strand composites in relation to the strand length," *Composite Structures*, 2018.

[30] I. R. Cole, *Modelling CPV*. Doctoral thesis, Loughborough University, 2015.

[31] J. S. Cintra and C. L. Tucker, "Orthotropic closure approximations for flow-induced fiber orientation," *Journal of Rheology*, vol. 39, no. 6, pp. 1095–1122, 1995.

[32] S. Pinho, R. Darvizeh, P. Robinson, C. Schuecker, and P. Camanho, "Material and structural response of polymer-matrix fibre-reinforced composites," *Journal of Composite Materials*, vol. 46, no. 19-20, pp. 2313–2341, 2012.

[33] E. J. Barbero, *Introduction to Composite Materials Design*. Taylor & Francis Group, 2nd ed., 2011.

[34] M. Zako, Y. Uetsuji, and T. Kurashiki, "Finite element analysis of damaged woven fabric composite materials," *Composites Science and Technology*, vol. 63, no. 3, pp. 507 – 516, 2003.

[35] Hexcel, "HexPly M77 Product Data." `https://www.hexcel.com/Resources/DataSheets/Prepreg`, 2017. [Online; accessed 04-April-2019].

[36] Mitsubishi Chemical Corporation, "TR50s Datasheet." `http://mccfc.com/pan-fiber/`. [Online; accessed 04-April-2019].

[37] A. Kaddour and M. Hinton, "Maturity of 3d failure criteria for fibre-reinforced composites: Comparison between theories and experiments: Part b of wwfe-ii," *Journal of Composite Materials*, vol. 47, no. 6-7, pp. 925–966, 2013.

[38] B. R. Denos, S. S. Kravchenko, and R. B. Pipes, "Progressive Failure Analysis in Platelet Based Composites Using CT-Measured Local Microstructure," in *International SAMPE Technical Conference*, (Seattle (WA)), 22-25 May, 2017.

[39] M. Selezneva and L. Lessard, "Characterization of mechanical properties of randomly oriented strand thermoplastic composites," *Journal of Composite Materials*, vol. 50, pp. 2833–2851, 2016.

[40] P. Feraboli, E. Peitso, F. Deleo, T. Cleveland, and P. B. Stickler, "Characterization of Prepreg-Based Discontinuous Carbon Fiber/Epoxy Systems," *Journal of Reinforced Plastics and Composites*, vol. 28, pp. 1191–1214, may 2009.

[41] D. E. Sommer, S. G. Kravchenko, and R. B. Pipes, "A numerical study of the meso-structure variability in the compaction process of prepreg platelet molded composites," *Composites Part A: Applied Science and Manufacturing*, vol. 138, p. 106010, 2020.

[42] S. Kravchenko and B. Pipes, "Virtual tensile testing of prepreg platelet composite molded with stochastic morphology," Sampe 2018, Long Beach, CA.

[43] Z. Chen, T. Huang, Y. Shao, Y. Li, H. Xu, K. Avery, D. Zeng, W. Chen, and X. Su, "Multiscale finite element modeling of sheet molding compound (smc) composite structure based on stochastic mesostructure reconstruction," *Composite Structures*, vol. 188, pp. 25–38, 2018.

[44] S. Ko, J. Davey, S. Douglass, J. Yang, M. E. Tuttle, and M. Salviato, "Effect of the thickness on the fracturing behavior of discontinuous fiber composite structures," *Composites Part A: Applied Science and Manufacturing*, vol. 125, p. 105520, 2019.

[45] H. C. Tseng, R. Y. Chang, and C. H. Hsu, "Improved fiber orientation predictions for injection molded fiber composites," *Composites Part A: Applied Science and Manufacturing*, vol. 99, pp. 65–75, 2017.

[46] G. Alnersson, M. W. Tahir, A.-L. Ljung, and T. S. Lundström, "Review of the numerical modeling of compression molding of sheet molding compound," *Processes*, vol. 8, no. 2, 2020.

[47] J. Teuwsen, S. K. Hohn, and T. A. Osswald, "Direct fiber simulation of a compression molded ribbed structure made of a sheet molding compound with randomly oriented carbon/epoxy prepreg strands—a comparison of predicted fiber orientations with computed tomography analyses," *Journal of Composites Science*, vol. 4, no. 4, 2020.

[48] S. Pimenta and P. Robinson, "An analytical shear-lag model for composites with 'brick-and-mortar' architecture considering non-linear matrix response and failure," *Composites Science and Technology*, vol. 104, pp. 111–124, 2014.

[49] J. Henry and S. Pimenta, "Virtual testing framework for hybrid aligned discontinuous composites," *Composites Science and Technology*, vol. 159, pp. 259–272, 2018.

[50] Y. Li, S. Pimenta, M. Thierry, and W. Y. Tan, "Prediction of stiffness for tow-based discontinuous composites.," in *ECCM17, Munich, Germany*, June 2016.